

# Coupling of magnetic order to planar Bi electrons in the anisotropic Dirac metals $AMnBi_2$ ( $A = Sr, Ca$ )

Y. F. Guo,<sup>1</sup> A. J. Princep,<sup>1</sup> X. Zhang,<sup>2</sup> P. Manuel,<sup>3</sup> D. Khalyavin,<sup>3</sup> I. I. Mazin,<sup>4</sup> Y. G. Shi,<sup>2,\*</sup> and A. T. Boothroyd<sup>1,†</sup>

<sup>1</sup>*Department of Physics, University of Oxford, Clarendon Laboratory,  
Parks Road, Oxford, OX1 3PU, United Kingdom*

<sup>2</sup>*Beijing National Laboratory for Condensed Matter Physics,*

*Institute of Physics, Chinese Academy of Sciences, Beijing 100190, China*

<sup>3</sup>*ISIS Facility, Rutherford Appleton Laboratory, Chilton, Didcot, OX11 0QX, United Kingdom*

<sup>4</sup>*Naval Research Laboratory, code 6390, 4555 Overlook Avenue SW, Washington DC 20375, USA*

(Dated: October 29, 2018)

We report powder and single crystal neutron diffraction measurements of the magnetic order in  $AMnBi_2$  ( $A = Sr$  and  $Ca$ ), two layered manganese pnictides with anisotropic Dirac fermions on a Bi square net. Both materials are found to order at  $T_N \approx 300$  K in  $\mathbf{k} = 0$  antiferromagnetic structures, with ordered Mn moments at  $T = 10$  K of approximately  $3.8 \mu_B$  aligned along the  $c$  axis. The magnetic structures are Néel-type within the Mn–Bi layers but the inter-layer ordering is different, being antiferromagnetic in  $SrMnBi_2$  and ferromagnetic in  $CaMnBi_2$ . This allows a mean-field coupling of the magnetic order to Bi electrons in  $CaMnBi_2$  but not in  $SrMnBi_2$ . We find clear evidence that magnetic order influences electrical transport. First principles calculations explain the experimental observations and suggest that the mechanism for different inter-layer ordering in the two compounds is the competition between the antiferromagnetic superexchange and ferromagnetic double exchange carried by itinerant Bi electrons.

PACS numbers: 71.20.Ps; 75.25.-j; 74.70.Xa; 75.30.Gw;

## I. INTRODUCTION

Dirac materials are a new class of quasi-two-dimensional electron systems whose properties are dominated by quasiparticles (Dirac fermions) whose energy disperses linearly with momentum. In isotropic Dirac materials, such as graphene,  $d$ -wave superconductors and topological insulators, the crossing of linearly dispersing bands at the Dirac point forms a Dirac cone. This, together with the well defined helicity of the states near the Dirac point, is responsible for the interesting and unusual behavior observed in Dirac materials, especially their transport properties in an external magnetic field<sup>1,2</sup>.

Recently, the layered manganese pnictides  $AMnBi_2$ , with  $A = Sr$  and  $Ca$ , were reported to exhibit anomalous metallic behavior consistent with a highly anisotropic Dirac dispersion and a sizable gap at the Dirac point due to spin-orbit coupling<sup>3,4</sup>. These compounds are structurally similar to the iron-based superconductors<sup>5,6</sup> and to novel dilute magnetic semiconductors<sup>7</sup>. They contain a layer of Mn–Bi composed of edge-sharing tetrahedra, and a Bi square net, separated by a layer of  $A$  atoms. Depending on  $A$ , the Mn–Bi layers can be stacked with or without a translation through  $(0.5, 0.5, 0)$ , forming correspondingly the  $I4/mmm$  or  $P4/nmm$  symmetry groups. First principles density function theory (DFT) band calculations<sup>3,4,8,9</sup> indicate that Mn is divalent, has five  $d$  electrons that are fully spin-polarized, and that the Dirac states, as well as other bands crossing the Fermi level, arise from the crossing of folded Bi  $6p_{x,y}$  bands in the doubled Bi square net of  $AMnBi_2$ . Interestingly, the Dirac cones are highly anisotropic in the  $xy$  plane, due to weak hybridization with  $A$  site

$d_{xy,yz}$  orbitals. A substantial amount of experimental evidence for anisotropic Dirac fermions in the Bi layer exists from measurements of magnetization, magnetotransport, angle-resolved photoemission spectra (ARPES) and magnetothermopower<sup>3,4,8,10–13</sup>. Other bands predicted by DFT are also seen in ARPES.

A further interesting feature of the  $AMnBi_2$  Dirac materials is the presence of antiferromagnetic (AFM) order, indicated by anomalies in the susceptibility at temperatures just below room temperature ( $SrMnBi_2$ : Refs. 3 and 8;  $CaMnBi_2$ : Refs. 4 and 11). Magnetism is potentially important in Dirac materials because long-range magnetic order could couple to the Dirac fermions and influence electrical transport. DFT calculations for  $AMnBi_2$ <sup>3,4,8,9</sup> indicate that the ordered moment is carried by the Mn atoms and is approximately  $4 \mu_B$  in magnitude, hybridization-reduced from the value of  $5 \mu_B$  expected for localized  $Mn^{2+}$  ( $3d^5, S = 5/2$ ). Strong in-plane superexchange leads to Néel-type antiferromagnetism in the  $ab$  plane, and the sense of the anisotropy in the susceptibility observed in the AFM phase suggests that the moments point parallel to the  $c$  axis. There are no predictions for the propagation of the magnetic structure along the  $c$  axis. The inter-layer magnetic coupling should be weak, and its sign is hard to predict from general considerations.

Here we report a neutron diffraction and electrical transport study in which we establish the three-dimensional magnetic structures of  $SrMnBi_2$  and  $CaMnBi_2$  and observe an anomaly at the AFM transition in the resistivity of  $CaMnBi_2$ , but not  $SrMnBi_2$ . We find Néel-type AFM order within the Mn–Bi layers with a reduced moment, consistent with previous

	CaMnBi <sub>2</sub>	SrMnBi <sub>2</sub>
Ca/Sr	25.1(0.3)	25.6(0.3)
Mn	25.4(0.2)	26.6(0.3)
Bi	49.5(0.4)	47.8(0.5)
	100%	100%

TABLE I. Electron-probe microanalysis (EPMA) of the composition of CaMnBi<sub>2</sub> and SrMnBi<sub>2</sub> single crystals. The results are given in atom %, and are averages over 10 (CaMnBi<sub>2</sub>) or 12 (SrMnBi<sub>2</sub>) points on the crystal surface. The standard deviations, given in parentheses, show the compositional spread and indicate the experimental error.

DFT calculations, but we find two different ordering sequences in the out-of-plane direction: antiferromagnetic in SrMnBi<sub>2</sub> and ferromagnetic in CaMnBi<sub>2</sub>. This means that coupling between the Mn magnetic order and the Bi square net (responsible for the electronic transport) is allowed at the mean field level in CaMnBi<sub>2</sub> but not in SrMnBi<sub>2</sub>, consistent with the behavior of the resistivity. Our first principles DFT calculations reproduce the observed inter-layer magnetic order and suggest a microscopic explanation for the differences in the magnetic order and behavior of the resistivity between the two materials.

## II. EXPERIMENTAL AND COMPUTATIONAL DETAILS

Polycrystalline samples of CaMnBi<sub>2</sub> and SrMnBi<sub>2</sub> were prepared by solid-state reaction. Stoichiometric amounts of Mn (99.9%), Bi (99.99%), and either Ca (99.99%) or Sr (99.99%) were mixed, ground and packed into an alumina tube, which was then sealed in a quartz tube. The mixture was heated up to 700°C in 10 hrs, reacted at this temperature for 48 hrs, and finally quenched to room temperature. Single crystals were grown using a self-flux method similar to that described previously<sup>8,10</sup>. Starting materials of Ca or Sr (99.99%), Mn (99.9%), and excess Bi (99.99%) were mixed in a molar ratio of Sr:Mn:Bi = 1:1:8, and put into an alumina tube before sealing in a quartz tube. The mixture was heated up to 800°C in 10 hrs, held at this temperature for 5 hrs, then slowly cooled to 450°C at a rate of 3°C hr<sup>-1</sup>. The excess Bi flux was decanted at this temperature in a centrifuge. These materials are reactive in air so handling was carried out in an inert gas atmosphere as far as possible.

The crystals were confirmed as single phase by room temperature X-ray diffraction measurements on powdered crystals. To check their composition, electron-probe microanalysis (EPMA) was performed at 10–12 points on the clean surface of one crystal of each type. The measured cation ratios (in atom %) are given in Table I. Both crystals are very close to the ideal stoichiometry, although the data suggest a small (~2%) Bi

deficiency in SrMnBi<sub>2</sub>. The analysis also revealed oxygen on the surface which most likely formed during brief exposure to air.

Magnetic susceptibility measurements were performed with a Superconducting Quantum Interference Device (SQUID) magnetometer. The susceptibility was measured under zero-field-cooled (ZFC) and field-cooled (FC) conditions, with the measuring field applied either parallel or perpendicular to the *c*-axis. Measurements of the in-plane resistivity ( $\rho_{ab}$ ) were made by the standard 4-probe method. Neutron time-of-flight diffraction data were collected on 3 g powder samples of CaMnBi<sub>2</sub> and SrMnBi<sub>2</sub>, and on a 1 × 2 × 2 mm single crystal of SrMnBi<sub>2</sub>. The measurements were performed on the WISH diffractometer<sup>14</sup> at the ISIS Facility of the Rutherford Appleton Laboratory (UK).

First principles calculations were performed using the WIEN2k package<sup>15</sup>, including the Generalized Gradient Correction to the DFT and spin-orbit interaction, with *k*-point meshes up to 58 × 58 × 11. The magnetic field in all calculations was assumed to be parallel to *c*.

## III. RESULTS AND ANALYSIS

Figure 1 (upper panels) shows the temperature dependence of the anisotropic magnetic susceptibility of CaMnBi<sub>2</sub> and SrMnBi<sub>2</sub> measured with a field of  $H = 10$  kOe ( $\mu_0 H = 1$  Tesla) applied parallel to the *ab* plane ( $H \parallel ab$ ) and along the *c* axis ( $H \parallel c$ ). Both materials have similar susceptibility curves. There are anomalies at two temperatures  $T_1$  and  $T_2$ , where  $T_1 = 305 \pm 5$  K (CaMnBi<sub>2</sub>) and  $295 \pm 5$  K (SrMnBi<sub>2</sub>), and  $T_2 = 265 \pm 5$  K (CaMnBi<sub>2</sub>) and  $260 \pm 5$  K (SrMnBi<sub>2</sub>). These can be viewed on an expanded scale in the susceptibility insets. From our neutron diffraction data (see below) we identify  $T_1$  with the onset of antiferromagnetic order at the Néel temperature  $T_N$ . Below  $T_1 = T_N$  the susceptibility is strongly anisotropic, with  $\chi_c < \chi_{ab}$ . Below  $T_2$  there is a prominent splitting between ZFC and FC measurements for  $H \parallel c$ . The  $T_1$  and  $T_2$  anomalies have both been reported previously for SrMnBi<sub>2</sub> (Ref. 8), but only the  $T_2$  anomaly has been reported before now for CaMnBi<sub>2</sub>. In common with previous data,<sup>3,8</sup> the susceptibility of SrMnBi<sub>2</sub> shows a strong Curie contribution at low temperatures. This indicates the presence of a small amount of Mn-containing paramagnetic impurity which might be related to the slight Bi deficiency indicated by EPMA (Table I).

Measurements of the in-plane resistivity ( $\rho_{ab}$ ) of two different samples of each material are presented in Fig. 1 (lower panels). The data for samples 1 and 2 of each material are broadly consistent with one another and with previous studies,<sup>3,4,8,10–12</sup>, but there are differences in some details. Firstly, our measurements, which extend above 300 K, reveal a bump at  $T_1 = 305$  K for CaMnBi<sub>2</sub> which is not present in the data for SrMnBi<sub>2</sub>. The anomaly is particularly sharp for sample 1, but is

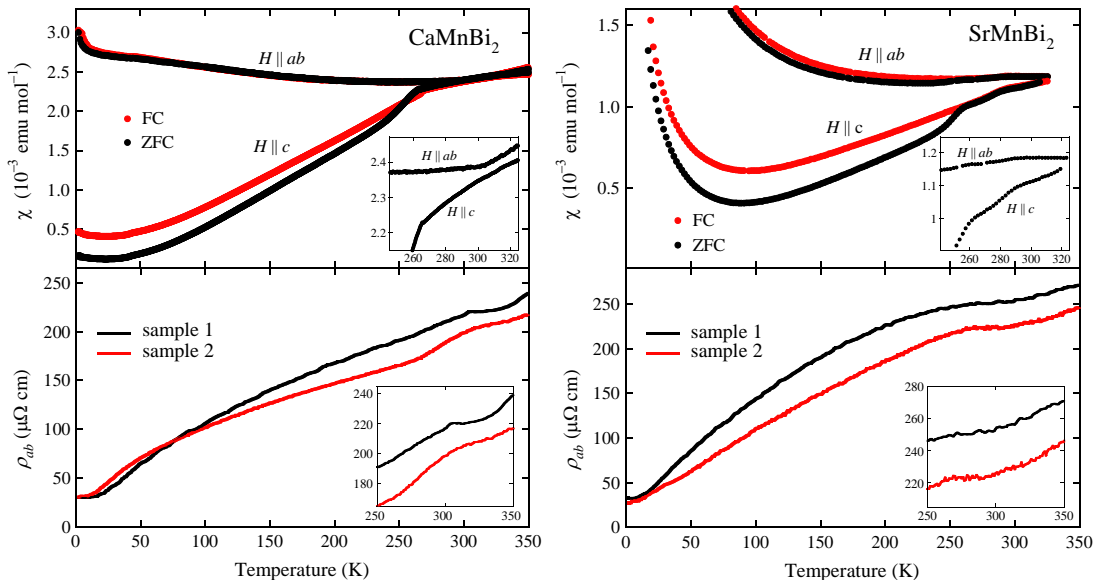


FIG. 1. (Color online) Temperature dependence of the susceptibility and resistivity of  $\text{CaMnBi}_2$  and  $\text{SrMnBi}_2$ . The susceptibility (upper panels) was measured under zero-field-cooled (ZFC) and field-cooled (FC) conditions in a field of  $H = 10 \text{ kOe}$  ( $\mu_0 H = 1 \text{ Tesla}$ ) applied parallel to the  $ab$  plane ( $H \parallel ab$ ) and along the  $c$  axis ( $H \parallel c$ ). The susceptibility insets show the ZFC data on an expanded scale in the vicinity of the magnetic anomalies at  $T_1 \approx 300 \text{ K}$  and  $T_2 \approx 260 \text{ K}$ . The in-plane resistivity (lower panels) was measured on two different samples for each material. The resistivity insets show the data on an expanded scale in the vicinity of the magnetic anomalies.

present for both samples of  $\text{CaMnBi}_2$ . The resistivity of the  $\text{SrMnBi}_2$  samples is smoother around room temperature with a small positive curvature that contrasts with the bump in the  $\text{CaMnBi}_2$  data. Second, there also appear to be features near  $T_2$  in the resistivity of sample 2 of both materials. However, the curves for samples 1 and 2 are not consistent in this temperature range, and there are no corresponding features near  $T_2$  in previous data for  $\text{CaMnBi}_2$  or  $\text{SrMnBi}_2$ . We assume, therefore, that these features are not intrinsic, and speculate that they could be effects due to the contacts. Finally, there have been reports of an anomaly in the resistivity of  $\text{CaMnBi}_2$  between 40 and 50 K.<sup>4,11,12</sup> However, no corresponding anomalies in the heat capacity have been reported, and we do not observe such an anomaly in our data.

The neutron powder diffraction pattern of  $\text{CaMnBi}_2$  collected in the paramagnetic phase at  $T = 310 \text{ K}$  was fitted with the structural model proposed by Brechtel *et al.*<sup>16</sup>. The model implies tetragonal  $P4/nmm$  symmetry with Mn occupying  $2a$  Wyckoff sites at  $3/4, 1/4, 0$  and  $1/4, 3/4, 0$  in the unit cell. The room temperature lattice parameters were refined as  $a = 4.4978(1) \text{ \AA}$  and  $c = 11.0692(6) \text{ \AA}$ , where the numbers in parentheses are fitting errors (one standard deviation). Below  $T_N$  additional scattering appears as illustrated in Fig. 2(a), left panel, revealing the onset of magnetic ordering with a  $\mathbf{k} = 0$  propagation vector. The lack of a magnetic contribution to the (001) reflection, Fig. 2(a), right panel, implies that the magnetic moments point along the  $c$ -axis, and the strong magnetic intensity at the nuclear-

forbidden (100) reflection points to an antiferromagnetic coupling between the two symmetry-related Mn sites.

These observations unambiguously determine the magnetic structure shown in Fig. 4 (left). The model has antiferromagnetic in-plane and ferromagnetic out-of-plane coupling between the nearest neighbors, and is described by the  $P4'/n'm'm$  magnetic space group. The refined value of the moment size is  $3.73(5) \mu_B$  at  $T = 10 \text{ K}$ , and the temperature dependence of the moment is shown in Fig. 2(b). The AFM ordering temperature in our sample,  $T_N = 300 \pm 5 \text{ K}$ , is consistent with the susceptibility and resistivity anomalies at  $T_1$  (Fig. 1), identifying  $T_1$  with the Néel temperature  $T_N$ .  $T_N$  of  $\text{CaMnBi}_2$  is therefore  $\sim 30 \text{ K}$  higher than previously reported based only on susceptibility data<sup>4,11</sup>.

Initial neutron powder diffraction measurements on  $\text{SrMnBi}_2$  revealed a number of candidate magnetic peaks. Subsequently, single crystal neutron diffraction data on  $\text{SrMnBi}_2$  were collected in two scattering geometries to access the  $(H, K, 0)$  and  $(H, 0, L)$  scattering planes. Room temperature lattice parameters refined in the  $I4/mmm$  space group were found to be  $a = 4.5771(2) \text{ \AA}$  and  $c = 23.14069(5) \text{ \AA}$ . Regions of the  $(H, 0, L)$  plane measured at temperatures of 10 K and 320 K are shown in Figs. 3(a) and (b), respectively. A strong magnetic contribution to the nuclear reflections along the  $(1, 0, L)$  line was observed at  $T = 10 \text{ K}$ , see Fig. 3(c). The magnetic intensity is resolution-limited and decreases with increasing scattering vector as expected due to the magnetic form factor. Based on this observation, a magnetic

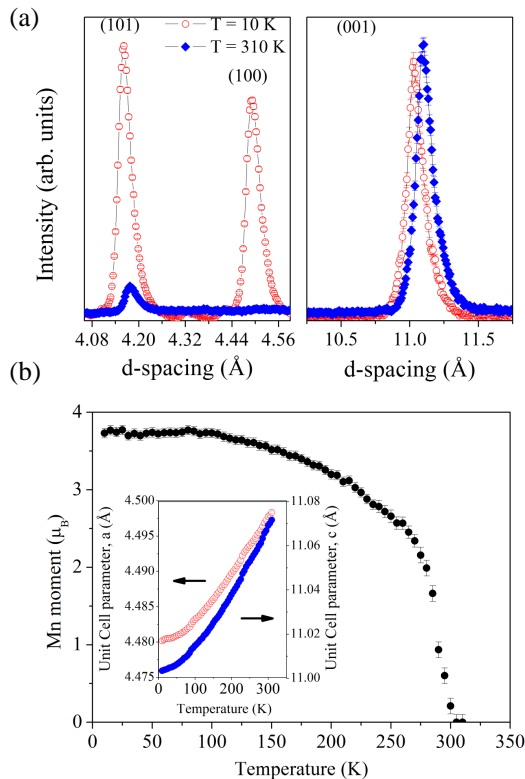


FIG. 2. (Color online) Neutron powder diffraction data for  $\text{CaMnBi}_2$ . (a) Left panel: (100) and (101) magnetic Bragg peaks at 10 K and 310 K. Right panel: (001) structural Bragg peak at 10 K and 310 K showing absence of a magnetic contribution. (b) Temperature dependence of the refined magnetic moment. The insert shows the temperature dependence of the  $a$  and  $c$  lattice parameters.

ordering of the Mn sublattice with the propagation vector  $\mathbf{k} = 0$  can be concluded. Inspection of the  $(H00)$ ,  $(0K0)$  and  $(00L)$  reflections did not reveal any magnetic contributions, Fig. 3(d). The slightly larger intensity of the (200) reflection at 10 K is of structural origin (uncorrelated atomic displacements) since the same thermal effect is observed for the (400) reflection (not shown).

To obtain a model for the magnetic structure of  $\text{SrMnBi}_2$  we adopted a symmetry-based approach, analysing the magnetic reflection conditions for the possible magnetic space groups. The parent symmetry was assumed to be  $I4/mmm$ , as determined by Cordier and Schäfer<sup>17</sup>. The magnetic space groups associated with  $\Gamma$ -point ( $\mathbf{k} = 0$ ) were generated by the ISOTROPY software<sup>18,19</sup> for the irreducible representations entering the pseudovector reducible representation on the  $4d$  Mn position. Then, the extinction rules for the magnetic space groups tabulated in the Bilbao Crystallographic Server (MAGNEXT<sup>20</sup>) for non-polarized neutron diffraction were applied, resulting in the unambiguous choice of  $I4'/m'm'm$  as the appropriate magnetic symmetry for  $\text{SrMnBi}_2$ . This space group is associated with the one-

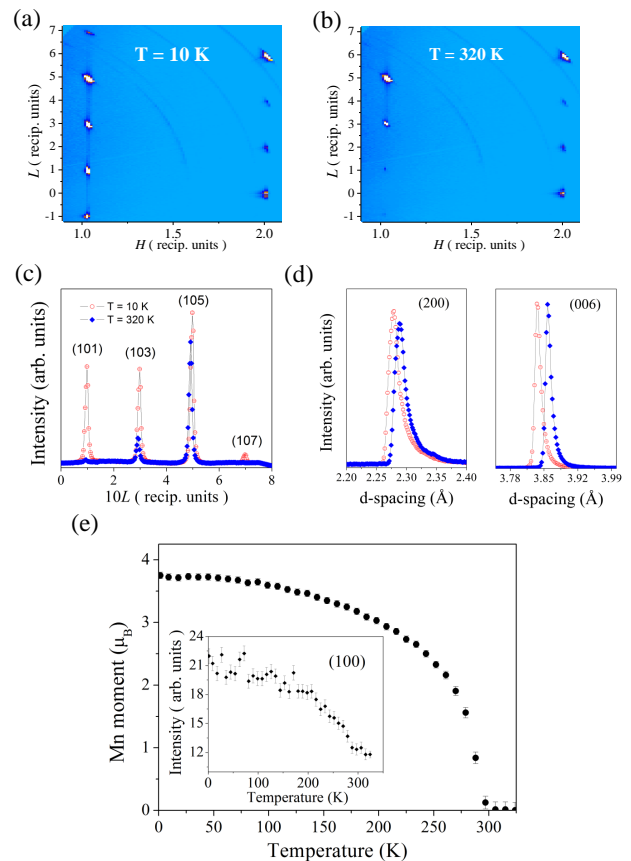


FIG. 3. (Color online) Neutron single-crystal diffraction data for  $\text{SrMnBi}_2$ . Diffraction peaks in the  $(H, 0, L)$  scattering plane at (a)  $T = 10$  K and (b)  $T = 320$  K. (c) Line scan along  $(1, 0, L)$  at 10 K and 320 K, showing additional magnetic intensity in the magnetically ordered phase. (d) (200) and (006) reflections showing absence of a magnetic contribution to these peaks. (e) Temperature dependence of the refined magnetic moment. The insert shows the temperature dependence of the weak (100) magnetic reflection.

dimensional  $\Gamma_2^-$  irreducible representation and implies an antiferromagnetic arrangement for both the in-plane and out-of-plane nearest neighbours with the spin direction along the  $c$ -axis, as shown in Fig. 4 (right). The refined value of the magnetic moment at  $T = 10$  K is  $3.75(5) \mu_B$ , and the temperature dependence of the moment is shown in Fig. 3(e). The AFM ordering temperature  $T_N = 295 \pm 5$  K is consistent with previous reports<sup>3,8</sup> and with the value of  $T_1$  from the magnetic susceptibility. The saturated moment is the same to within experimental error as we find in  $\text{CaMnBi}_2$ . Thus, the main difference between the magnetic structures of  $\text{CaMnBi}_2$  and  $\text{SrMnBi}_2$  is the sign of the out-of-plane coupling: ferromagnetic for the former, antiferromagnetic for the latter.

In addition to the  $\mathbf{k} = 0$  magnetic peaks, we observed a very small (100) reflection in the data for  $\text{SrMnBi}_2$ . The (100) is forbidden in the  $I$ -centered lattice, and is only

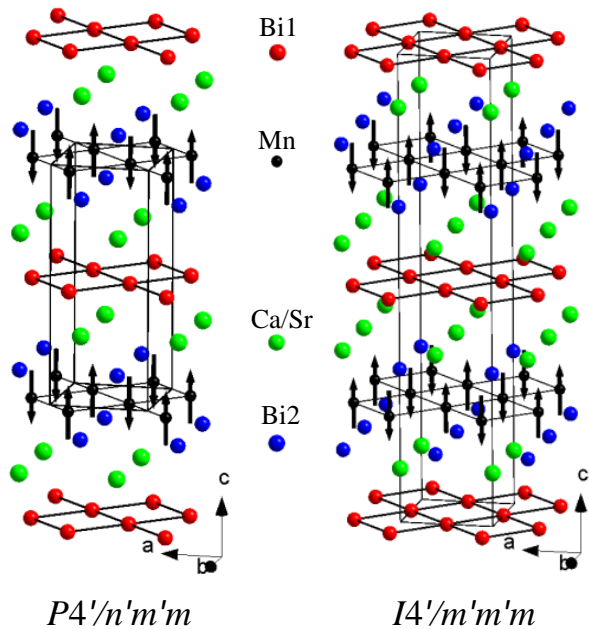


FIG. 4. (Color online) Magnetic structures of  $\text{CaMnBi}_2$  (left) and  $\text{SrMnBi}_2$  (right).

observed at  $T < T_N$  — see insert to Fig. 3(e). This observation indicates the existence of a structural distortion with wave vector  $\mathbf{k} = (1, 1, 1)$ . If the magnetic transition is continuous, as suggested by Fig. 3(e), then either (i) there exists a structural instability unrelated to the magnetic order that occurs very close to (but not coincident with)  $T_N$ , or (ii) the primary  $\mathbf{k} = 0$  magnetic order parameter induces (via a trilinear free energy invariant) a secondary magnetic mode with  $\mathbf{k} = (1, 1, 1)$  due to the existence already in the paramagnetic phase of a structural distortion also with  $\mathbf{k} = (1, 1, 1)$ . Group theoretical analysis shows that in the latter case the symmetry of the paramagnetic phase would have to be  $P4/nmm$ ,  $Cmcm$  or  $Pmnm$ . However, we failed to find any direct evidence that the high-temperature structure is other than  $I4/mmm$ .

Next, we describe the results of the band structure calculations. Figures 5(a) and (b) show the Fermi surfaces of both compounds calculated with antiferromagnetic order in the plane and ferromagnetic stacking along  $c$  (denoted “AF-fz”). Figures 5(c) and (d) show likewise for antiferromagnetic stacking (“AF-az”). For the sake of comparison, we used for both compounds a tetragonal cell containing two Mn layers, corresponding to one ( $\text{SrMnBi}_2$ ) and two ( $\text{CaMnBi}_2$ ) of the unit cells depicted in Fig. 4.

To illustrate the band structure in the vicinity of the

Fermi energy,  $E_F$ , we show in Fig. 6 the calculated band dispersion of  $\text{CaMnBi}_2$  for energies in the range  $E_F \pm 0.4 \text{ eV}$  for the case of ferromagnetic stacking. The results are consistent with earlier calculations.<sup>4,9</sup> (note that the bands in Fig. 6 are downfolded along  $k_z$  compared to those in Refs. 4 and 9). The Dirac cones are located between the  $\Gamma$  and M points, and are strongly squeezed in the (110) direction. Moreover, the Dirac points (though not the Dirac bands) are destroyed by the spin-orbit interaction (a  $k_z$ -dependent gaps opens with magnitude varying between 1.4 and 15 meV). At the same time, several other Fermi surface pockets, besides the Dirac ones, are also formed by the planar Bi electrons, but these have strong  $p_z$  character, as opposed to the  $p_{x,y}$ -derived Dirac bands.

To assess the relative importance of the Dirac and non-Dirac bands to the electronic transport we have calculated for  $\text{CaMnBi}_2$  the band-decomposed plasma frequencies  $\omega_p$ . In the constant scattering rate approximation the conductivity is proportional to  $\omega_p^2$ . We found that for the Dirac bands  $\omega_{px} = \omega_{py} = 2.45 \text{ eV}$ , and  $\omega_{pz} = 0.24 \text{ eV}$ . For the non-Dirac bands these numbers are 0.42 and 0.30 eV, respectively. Thus, the in-plane transport is dominated by the Dirac electrons (as opposed to the out-of-plane one). Unfortunately, it is harder to decompose the plasma frequency for  $\text{SrMnBi}_2$  in a similar way, because some of the Dirac bands have the same band number as the 3D bands (cf. the colors in Fig. 5).

Interestingly, switching from ferromagnetic to antiferromagnetic inter-layer stacking has a rather distinct effect on the fermiology of the two compounds. In  $\text{SrMnBi}_2$ , the Fermi surface is virtually insensitive to the type of stacking, whereas in  $\text{CaMnBi}_2$  there is a clear difference in the bands near  $E_F$  for the two types of stacking. This difference can be seen in the Fermi surfaces, Fig. 5, and in the stacking-dependent band dispersions shown in Fig. 7. The strongest effect is seen on the three-dimensional Fermi surface pocket near  $\Gamma$ . One can also see that for  $\text{CaMnBi}_2$  the dispersion of this band along  $z$  is higher in the fz structure (by  $\approx 10\%$ ) than in the az one, whereas for  $\text{SrMnBi}_2$  the same band is very similar for the fz and az structures. This feature could prove important in the energetics, as discussed below. These results indicate that the bands near  $E_F$  couple more strongly to the inter-layer magnetic order in  $\text{CaMnBi}_2$  than in  $\text{SrMnBi}_2$ , in agreement with the experimental observation of a resistivity anomaly at  $T_N$  for  $\text{CaMnBi}_2$ , but not for  $\text{SrMnBi}_2$ .

We have calculated the energy difference between the two different magnetic stackings in both compounds. Independently of the stacking, we found the moment inside the muffin-tin sphere of Mn (radius  $1.3 \times 10^{-10} \text{ m}$ ) to be  $4.03 \mu_B$  for  $\text{SrMnBi}_2$  and  $3.97 \mu_B$  for  $\text{CaMnBi}_2$ . The deviation from experiment is about 7%, which tells us that fluctuations beyond the mean field are weak (compared for example with the Fe pnictides where the deviation is close to a factor of two). We found that the energy difference per Mn is 1.2 meV for  $\text{CaMnBi}_2$ , in favor of the

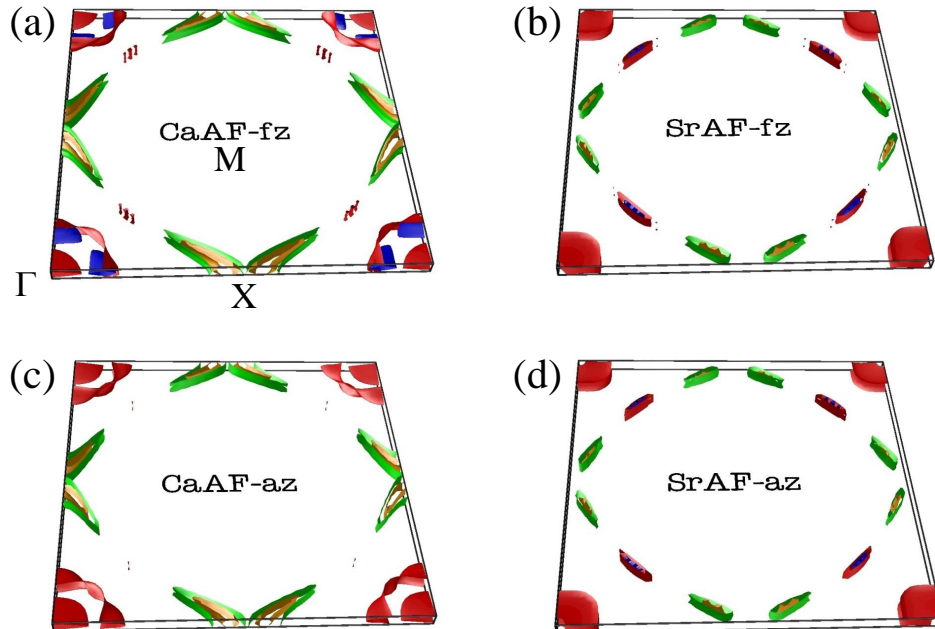


FIG. 5. (Color online) Calculated Fermi surfaces of  $\text{CaMnBi}_2$  and  $\text{SrMnBi}_2$  with Néel ordering in the plane and either ferromagnetic inter-layer stacking, (a) and (b), denoted “AF-fz”, or antiferromagnetic stacking, (c) and (d), denoted “AF-az”. Note that the Fermi surface of  $\text{SrMnBi}_2$  is virtually sensitive to the stacking, but that of  $\text{CaMnBi}_2$  is not.

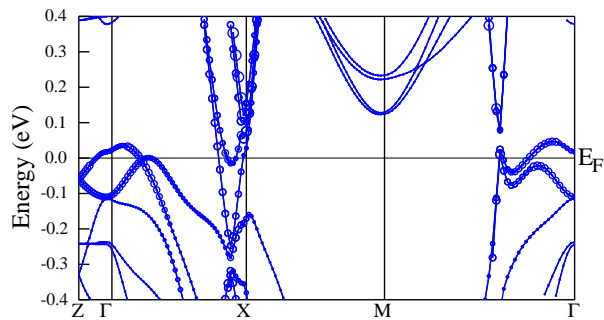


FIG. 6. (Color online) Band structure of  $\text{CaMnBi}_2$  calculated with ferromagnetic stacking (AF-fz). The size of the circles represents the contribution from the Bi  $6p_{x,y}$  orbitals.

ferromagnetic stacking, and 1.5 meV for  $\text{SrMnBi}_2$ , in favor of the antiferromagnetic stacking, both in agreement with experiment. We have also calculated the energy cost of aligning all spins ferromagnetically and found it to be extremely high, on the order of 300 meV per Mn for both compounds, suggesting that these systems are magnetically extremely two-dimensional, and that the relatively low ordering temperature is due to the logarithmic suppression of the Néel temperature due to inter-layer fluctuations.

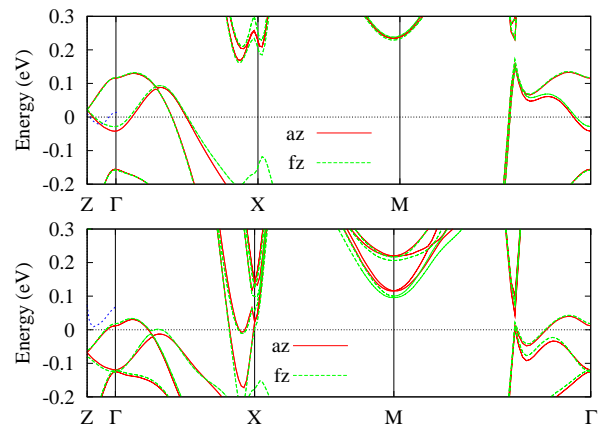


FIG. 7. (Color online) Effect of ferromagnetic *vs* antiferromagnetic stacking on the band structure of  $\text{SrMnBi}_2$  (upper panel) and  $\text{CaMnBi}_2$  (lower panel). The dotted (blue) lines between  $\Gamma$  and Z represent the difference between the fz and az bands multiplied by 10 to emphasize the stacking-dependent broadening of the three-dimensional Bi band near  $\Gamma$  for  $\text{CaMnBi}_2$  relative to  $\text{SrMnBi}_2$ .

We have established that the coupling of the three-dimensional Bi bands to the Mn magnetic order is stronger in  $\text{CaMnBi}_2$  than  $\text{SrMnBi}_2$ . But why is there

a reversal of the inter-layer interaction? First, one may think about the Hund's coupling on the planar Bi. Indeed, in the fz configuration the Bi is allowed to acquire a magnetic moment, thus gaining magnetic energy of  $M_{\text{Bi}}^2 I_{\text{Bi}}/4$ , where  $I_{\text{Bi}} \lesssim 1$  eV is the Stoner parameter for Bi. Indeed, Bi does acquire a magnetic moment, and according to our calculations it is a factor of 2 larger in  $\text{CaMnBi}_2$  than in  $\text{SrMnBi}_2$  ( $0.007 \mu_{\text{B}}$  vs.  $0.003 \mu_{\text{B}}$ ), but the corresponding energy gain is less than  $20 \mu\text{eV}$ , not enough by far to explain the effect.

We propose instead that the ferromagnetic interaction between the layers in  $\text{CaMnBi}_2$  is similar in nature to double exchange and to ferromagnetism in dilute magnetic semiconductors. The fact that the relevant Bi band becomes some 10% wider in the ferromagnetically-stacked  $\text{CaMnBi}_2$  indicates better delocalization of the corresponding electrons and therefore a gain in their kinetic energy. The order of magnitude of this effect can be obtained from the number of holes in the  $\Gamma$ -centered Fermi surface pocket multiplied by the width of the relevant band. This rough estimate gives 3–5 meV, which is in the right ballpark. The virtual absence of any coupling of the Bi electrons to magnetism in  $\text{SrMnBi}_2$  suggests that the antiferromagnetic inter-layer coupling in  $\text{SrMnBi}_2$  is caused by superexchange. We conclude, therefore, that the inter-layer interaction comes about from competition between the antiferromagnetic standard superexchange and a double-exchange-like itinerant ferromagnetic interaction.

The latter interaction may not be very accurately described by a short-range Heisenberg interaction, but given its small amplitude this is not a bad model. In this case, the minimal model is the square 2+1D model,  $\mathcal{H} = \sum_{\text{nn}} J_{ab} S_i S_j + \sum_{\text{nnn}} J_c S_i S_j$ , where the former sum is taken over all nearest-neighbor (nn) bonds in the plane and the latter over all such bonds between the planes. From the energy differences between fz and az configurations we can deduce  $J_c S^2 = (E_{\text{fz}} - E_{\text{az}})/2 \sim \pm 0.7$  meV (there is one such bond per Mn). We can also estimate  $J_{ab}$  from the calculated energy difference between a ferromagnetic and an antiferromagnetic in-plane arrangement. We found this difference to be about 300 meV for both compounds, so that  $J_{ab} S^2 = (E_{\text{FM}} - E_{\text{AF}})/4 \approx 75$  meV.

There have been numerous studies of such 2+1D models. The Monte-Carlo simulations of Yasuda *et al.*<sup>21</sup>, consistent with the analytical results of Irkhin and Katanin<sup>22</sup>, suggest that for the ratio  $J_{ab}/|J_c| \sim 100$  the transition temperature is  $T_{\text{N}} \approx 0.7 J_{ab} S^2 / k_{\text{B}} \sim 600$  K. This is about twice larger than the experimental number, but is in fact very consistent with it: first, experimental moments are smaller than the calculated mean-field ones by about 7%, which suggests that the exchange energy scale is suppressed by fluctuations by some 15%, reducing  $T_{\text{N}}$  to  $\sim 500$  K. Second, the superexchange interaction is inversely proportional to the energy cost of moving a Mn electron to another atom while flipping its spin,  $\Delta_{\uparrow\downarrow}$ . This is routinely underestimated in DFT calcula-

tions because of insufficient account of the on-site Hubbard repulsion. For  $\text{Mn}^{2+}$  underestimation of 50–100% is common. To demonstrate that, we have performed calculations using the LDA+U formalism. In this formalism,  $\Delta_{\uparrow\downarrow} \approx 5I + U_{\text{eff}}$ , where  $U_{\text{eff}} = U - J_{\text{H}}$ . Here,  $I \lesssim 1$  eV is the DFT Stoner factor for Mn, and  $U$  and  $J_{\text{H}}$  are the Hubbard repulsion and the Hund's rule coupling on Mn. Indeed, we found that the energy difference between the ferromagnetic and antiferromagnetic states follows the same formula,  $J_{ab} \propto (5\text{eV} + U_{\text{eff}})^{-1}$ , and for a very reasonable choice of  $U_{\text{eff}} = 3$  eV we obtain  $T_{\text{N}} \approx 350$  K, in very good agreement with experiment.

Finally, we have calculated the magnetic anisotropy energy (the difference in energy between a spin pointing parallel and perpendicular to the layers) for  $\text{CaMnBi}_2$  (not including a  $U$ ), and found it to be  $K \approx 0.7$  meV per Mn, with the easy direction the  $c$  axis, in agreement with experiment. This value suggests a spin-flop transition at a field  $B_{\text{SF}} \approx 2\sqrt{K(E_{\text{FM}} - E_{\text{AF}})/(g\mu_{\text{B}}S)} \sim 100$ –125 T.

#### IV. CONCLUSIONS

The central experimental results of this work are, (i) that the Dirac materials  $\text{AMnBi}_2$  with  $A = \text{Sr}$  and  $\text{Ca}$  have Néel-type in-plane AFM order (ii) that the  $\text{MnBi}_4$  layers are coupled ferromagnetically in  $\text{CaMnBi}_2$  but antiferromagnetically in  $\text{SrMnBi}_2$ , and (iii) that the resistivity of  $\text{CaMnBi}_2$  (but not  $\text{SrMnBi}_2$ ) has an anomaly at  $T_{\text{N}}$ . The latter is consistent at the mean-field level with the different inter-layer magnetic couplings. This study also shows conclusively that the AFM ordering transition correlates with the  $T_1$  anomalies observed in the susceptibility.

The opposite inter-layer magnetic coupling in  $\text{SrMnBi}_2$  and  $\text{CaMnBi}_2$  is fully reproduced in the first principles calculations, and its origin is suggested to be a competition between antiferromagnetic superexchange and a ferromagnetic double-exchange-like interaction, the former winning in  $\text{SrMnBi}_2$  and the latter in  $\text{CaMnBi}_2$ . The ferromagnetic component, itinerant in origin, is due to a 3D band generated by the square-planar Bi electrons, whose mobility appears noticeably higher in the ferromagnetically-stacked  $\text{CaMnBi}_2$  than in the antiferromagnetically-stacked  $\text{SrMnBi}_2$ . Our calculations show that the Dirac fermions dominate the in-plane electrical transport in both materials, but magnetism couples largely to non-Dirac-like Bi electrons, consistent with the relatively small size of the resistivity anomaly observed at  $T_{\text{N}}$  in  $\text{CaMnBi}_2$ . It would be of interest to measure the inter-layer transport, which should show a larger effect at  $T_{\text{N}}$ .

The question of what causes the anomaly at  $T_2 \approx 260$  K corresponding to the FC–ZFC splitting in the susceptibility remains open. No heat capacity anomalies have been reported at  $T_2$ , and we could find no evidence for any magnetic or structural phase changes below  $T_{\text{N}}$  to within the sensitivity of our diffraction measurements

— see, for example, the insert to Fig. 2(b). Therefore, if these anomalies are the result of spin reorientations or structural distortions then the changes to the magnetic or lattice symmetry are very subtle. The FC–ZFC splitting at  $T_2$  is suggestive of domain formation or disorder which might result from inter-layer stacking faults frozen in at  $T_2$ . We have observed that there is additional diffuse scattering at 10 K compared with 300 K in the form of a rod of scattering along the  $(1, 0, L)$  line in reciprocal space — compare Figs. 3(a) and (b). This form of diffuse scattering is consistent with the existence of stacking faults along the  $c$  axis.

## ACKNOWLEDGMENTS

We thank Prof. K. Yamaura of the National Institute for Materials Science, Tsukuba, Japan, for performing the EPMA measurements. This work was supported by the U.K. Engineering and Physical Sciences Research Council. Work in Beijing was supported by the 973 project of the Ministry of Science and Technology of China (No. 2011CB921701) and the National Natural Science Foundation of China (No. 11274367). I.I.M. acknowledges funding from the Office of Naval Research (ONR) through the Naval Research Laboratory’s Basic Research Program.

- 
- \* ygshi@aphy.iphy.ac.cn  
† a.boothroyd@physics.ox.ac.uk
- <sup>1</sup> A. H. Castro Neto, F. Guinea, N. M. R. Peres, K. S. Novoselov, and A. K. Geim, *Rev. Mod. Phys.* **81**, 109 (2009).
  - <sup>2</sup> J. Cayssol, *C. R. Physique* **14**, 760 (2013).
  - <sup>3</sup> J. Park, G. Lee, F. Wolff-Fabris, Y. Y. Koh, M. J. Eom, Y. K. Kim, M. A. Farhan, Y. J. Jo, C. Kim, J. H. Shim, and J. S. Kim, *Phys. Rev. Lett.* **107**, 126402 (2011).
  - <sup>4</sup> K. Wang, D. Graf, L. Wang, H. Lei, S. W. Tozer, and C. Petrovic, *Phys. Rev. B* **85**, 041101(R) (2012).
  - <sup>5</sup> D. C. Johnston, *Adv. Phys.* **59**, 803 (2010).
  - <sup>6</sup> G. R. Stewart, *Rev. Mod. Phys.* **83**, 1589 (2011).
  - <sup>7</sup> Z. Deng, C. Q. Jin, Q. Q. Liu, X. C. Wang, J. L. Zhu, S. M. Feng, L. C. Chen, R. C. Yu, C. Arguello, T. Goko, F. Ning, J. Zhang, Y. Wang, A. A. Aczel, T. Munsie, T. J. Williams, G. M. Luke, T. Kakeshita, S. Uchida, W. Higemoto, T. U. Ito, B. Gu, S. Maekawa, G. D. Morris, and Y. J. Uemura, *Nature Comm.* **2**, 422 (2011); J. K. Glasbrenner, I. Zutic, and I. I. Mazin, arXiv:1405.2854.
  - <sup>8</sup> J. K. Wang, L. L. Zhao, Q. Yin, G. Kotliar, M. S. Kim, M. C. Aronson, and E. Morosan, *Phys. Rev. B* **84**, 064428 (2011).
  - <sup>9</sup> G. Lee, M. A. Farhan, J. S. Kim, and J. H. Shim, *Phys. Rev. B* **87**, 245104 (2013).
  - <sup>10</sup> K. Wang, D. Graf, H. Lei, S. W. Tozer, and C. Petrovic, *Phys. Rev. B* **84**, 220401(R) (2011).
  - <sup>11</sup> J. B. He, D. M. Wang, and G. F. Chen, *Appl. Phys. Lett.* **100**, 112405 (2012).
  - <sup>12</sup> K. Wang, L. Wang, and C. Petrovic, *Appl. Phys. Lett.* **100**, 112111 (2012).
  - <sup>13</sup> Y. Feng, C. Chen, Y. Shi, Z. Xie, H. Yi, A. Liang, S. He, J. He, Y. Peng, X. Liu, Y. Liu, L. Zhao, G. Liu, X. Dong, J. Zhang, C. Chen, Z. Xu, and X. J. Zhou, *Sci. Rep.* **4**, 5385 (2014).
  - <sup>14</sup> L. C. Chapon, P. Manuel, P. G. Radaelli, C. Benson, L. Perrott, S. Ansell, N. J. Rhodes, D. Raspino, D. Duxbury, E. Spill, and J. Norris, *Neutron News*, **22**, 22 (2011).
  - <sup>15</sup> P. Blaha, K. Schwarz, G. K. H. Madsen, D. Kvasnicka, and J. Luitz 2001 WIEN2k, *An Augmented PlaneWave+LocalOrbitals Program for Calculating Crystal Properties* (Karlheinz Schwarz, Techn. Universität Wien, Austria).
  - <sup>16</sup> E. Brechtel, G. Cordier, and H. Schäfer, *Z. Naturforsch. B* **35**, 1 (1980).
  - <sup>17</sup> G. Cordier and H. Schäfer, *Z. Naturforsch. B* **32**, 383 (1977).
  - <sup>18</sup> H. T. Stokes, D. M. Hatch, and B. J. Campbell, ISOTROPY Software Suite, [iso.byu.edu](http://iso.byu.edu) (2007).
  - <sup>19</sup> B. J. Campbell, H. T. Stokes, D. E. Tanner, and D. M. Hatch, *J. Appl. Cryst.* **39**, 607 (2006).
  - <sup>20</sup> S. V. Gallego, E. S. Tasci, G. de la Flor, J. M. Perez-Mato, and M. I. Aroyo, *J. Appl. Cryst.* **45**, 1236 (2012).
  - <sup>21</sup> C. Yasuda, S. Todo, K. Hukushima, F. Alet, M. Keller, M. Troyer, and H. Takayama, *Phys. Rev. Lett.* **94**, 217201 (2005).
  - <sup>22</sup> V. Yu. Irkhin and A. A. Katanin, *Phys. Rev. B* **55**, 12 318 (1997).